Journal of Materials Chemistry A

Accepted Manuscript

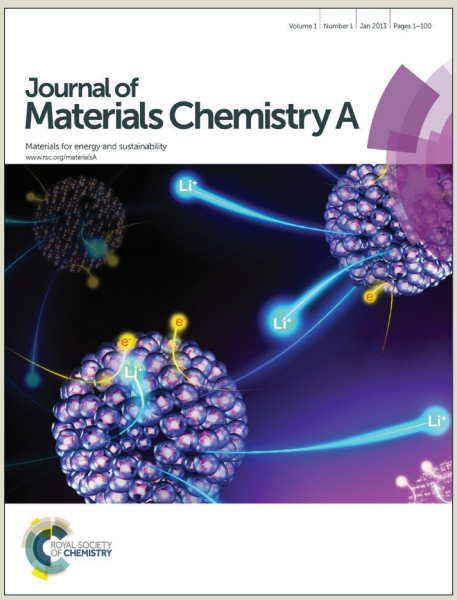

ROYAL SOCIETY OF CHEMISTRY

www.rsc.org/materialsA

Tuning oxygen content and distribution by substitution at Co site in 112 $YBaCo_2O_{5+\delta}$. Impact on transport and thermal expansion properties

A.S. Urusova[1], V.A. Cherepanov[1], O.I. Lebedev[2], T.V. Aksenova[1], L.Ya. Gavrilova[1], V. Caignaert[2], B. Raveau[2].

[1]*Department of Chemistry, Institute of Natural Sciences, Ural Federal University, Yekaterinburg, Russia*

[2]*Laboratoire CRISMAT, CNRS-Ensicaen , Université de Caen Basse Normandie, Caen, France*

Abstract

Polycrystalline "112" ordered oxygen deficient double perovskites $YBaCo_{2-x}Me_xO_{5+\delta}$ (Me=Fe, Cu, Ni) were synthesized by a glycerol-nitrate route, with $0.0 \le x \le 0.7$ for Me=Fe, $0.0 \le x \le 0.6$ for Me=Cu and x=0.1 for Me=Ni. The combined X-ray diffraction, electron microscopy and thermo-gravimetric study shows that all these oxides exhibit the $a_p \times a_p \times 2a_p$ tetragonal structure (S.G. *P4/mmm*) and that the oxygen content increases continuously with x in the iron substituted oxide $YBaCo_{2-x}Fe_xO_{5+\delta}$, whereas the opposite is observed for the copper phase $YBaCo_{2-x}Cu_xO_{5+\delta}$. This difference which is due to the more electropositive character of Fe^{3+} compared to Cu^{2+} is hindered in the Ni^{2+} case due to its inability to accommodate the pyramidal coordination. The particular evolution of the conductivity of these compounds versus temperature is closely related to their oxygen loss, in agreement with a defect structure model suggested earlier. Thermal expansion measurements prove the absence of phase transition in all oxides within the temperature range studied. Chemical compatibility of $YBaCo_{1.4}Fe_{0.6}O_{5+\delta}$ with the electrolyte $Ce_{0.8}Sm_{0.2}O_{2-\delta}$ is demonstrated.

Keywords: Solid oxide fuel cells, layered perovskite, cobaltates, crystal structure, X-ray diffraction, thermogravimety, thermal expansion.

Introduction

Perovskite type layered oxides based on rare earth elements, barium and cobalt became recently the subject of raised interest as cathode materials for the intermediate temperature-operating solid oxide fuel cells (IT-SOFCs) and ceramic oxygen membranes [1-3]. These oxides, called "112" belong to a large family of ordered oxygen deficient perovskites formulated $LnBaCo_2O_{5+\delta}$, where Ln is a rare earth element (Pr – Ho, Y), discovered twenty years ago [4, 5]. These oxides possess a number of properties, such as high

mixed electronic-ionic conductivity and fast oxygen diffusion [1-3, 6-7] that makes them attractive for applications as cathode materials. Nevertheless the oxygen content in these oxides is difficult to control and they reveal relatively high reactivity towards electrolyte materials. The high value of oxygen mobility in these systems is linked with the 1:1 ordering of the Ba^{2+} and Ln^{3+} species, which are stacked in the form of stoichiometric BaO layers and oxygen deficient LnO_{δ} layers alternately. As a consequence, various oxygen vacancy orderings while the oxygen content is changing can be generated within the LnO_{δ} layers, depending on the size difference between the Ba^{2+} and Ln^{3+} cations and on the conditions (temperature and oxygen partial pressure).

In fact, this structural behavior is not limited to pure cobaltates, since it was discovered for the first time in the oxide $LnBaFeCuO_5$ for which $\delta=0$ [8]. Recently, it was shown that Co in the $LnBaCo_2O_{5+\delta}$ lattice can be partially replaced by other 3d transition metals, such as Fe, Ni or Cu [9-16], leading to significant changes in oxygen content and ordering in those double perovskites. Despite the important role of the 3d-transition metal in the modification of the properties of these materials, its influence upon the oxygen stoichiometry/ordering is not fully understood, as illustrated for yttrium cobaltates [17-21].

In the present study of the oxides $YBaCo_{2-x}Me_xO_{5+\delta}$ (Me = Fe, Cu, Ni), we demonstrate that the substitution of a trivalent cation like iron for cobalt increases the oxygen content tending to form fully occupied [YO] layers, whereas in contrast the substitution of a divalent cation like copper decreases the oxygen content tending to form empty [Y] layers. Both substitutions change dramatically the oxygen ordering in the YO_{δ} layer, leading to an $a_p \times a_p \times 2a_p$ cell. The small homogeneity range for the Ni-substituted phase is also emphasized and explained by the disinclination of nickel ions to accommodate the pyramidal coordination. The transport properties and thermal behavior of these oxides are shown and discussed.

Experimental

Polycrystalline samples $YBaCo_{2-x}Me_xO_{5+\delta}$ (Me = Fe, Cu, Ni) with $0.0 \le x \le 1.0$ were synthesized by a glycerol–nitrate method. Yttrium oxide Y_2O_3, barium carbonate $BaCO_3$, copper oxide CuO, iron oxalate $FeC_2O_4 \times 2H_2O$, metallic cobalt and nickel with a purity not less than 99.5% were used as starting materials. The starting materials were preliminarily dried in air to remove adsorbed moisture and gases. Since the dissolution rate of cobalt oxide Co_3O_4 and nickel oxide NiO in the nitric acid was very slow they were preliminary transformed to the metal form. Metallic cobalt and nickel were prepared by the reduction of oxides Co_3O_4 and NiO, respectively, at 673–873 K in a hydrogen flow.

Raw mixtures with appropriate ratios of starting materials were dissolved in nitric acid, and then glycerin was added to the solution. The resulting gel was dried, decomposed at 573 K and burnt at various temperatures (673–1173 K). Final anneals of the $YBaCo_2O_{5+\delta}$ and $YBaCo_{2-x}Me_xO_{5+\delta}$ with Me = Fe and Ni were performed at 1373 K in air during 120 h with intermediate grindings in the agate mortar after each 20 h. Since the substitution of copper for cobalt leads to a decrease of melting temperature, the final annealing of the $YBaCo_{2-x}Cu_xO_{5+\delta}$ was performed at 1273 K in air during 120 h. Finally all samples were slowly cooled to room temperature at the rate 100 K/hour.

The phase composition and crystal structure of the samples were studied by powder X-ray diffraction (PXRD) analysis using DRON-6 instrument and Inel Equinox 3000 (CuK_α radiation). High temperature PXRD experiments were performed using the high temperature camera HTK 16N (Anton Paar GmbH, Austria). The values of unit cell parameters were calculated using "Celref 3" package, structural parameters were refined using Fullprof software [22, 23]. The intensity data for the Rietveld analysis were collected at each 0.02–0.04º by step for 7 or 10 s over the angular range $10°\leq 2\theta \leq 120°$. The convergence between experimental PXRD data and calculated profiles were estimated by a set of standard factors: R_p – the profile factor, R_f – the structural factor, R_{Br} – the Bragg-factor.

Crystal structure and chemical composition of as prepared $YBaCo_2O_{5+\delta}$ and $YBaCo_{2-x}Me_xO_{5+\delta}$ with Me = Fe, Cu (x=0.2-0.7) and Ni (x=0.1) samples were studied at local scale by means of transmission electron microscopy. Transmission electron microscopy (TEM), electron diffraction (ED) and high resolution TEM (HRTEM) studies were carried out using a FEI Tecnai G2 30 UT microscope operated at 300 kV and having 0.17 nm point resolution and equipped with EDAX EDX detector. The TEM specimens were prepared by grinding the material with methanol in an agate mortar, and spreading it out on a copper holey carbon grid.

Thermogravimetric measurements (TGA) were carried out using STA 409 PC Netzsch GmbH (weight resolution of 1 μg; sample weight of 1–1.5 g) within the temperature range 298 - 1373 K in air in dynamic (heating/cooling rate of 1–2 K/min) and static regimes (stepwise heating/cooling with soaking at each temperature during 8 h).

The values of oxygen content for $YBaCo_{2-x}Fe_xO_{5+\delta}$ (x=0; 0.2; 0.4; 0.6 and 0.7) were determined by means of reduction of the samples inside the TGA cell in a flow of dried 10 vol. % H_2–90 vol. % Ar mixture at 1273 K for 10 h. The accuracy of the oxygen index determination was not less than ± 0.01.

The average oxidation state of Co and room-temperature oxygen content values in $YBaCo_{2-x}Me_xO_{5+\delta}$ (Me=Cu, Ni) were determined by iodometric titration [24]. The samples, with weights of 0.1–0.2 g, were dissolved in HCl in the presence of KI, and then, the obtained solution was titrated with a thiosulfate solution. The concentration of $Na_2S_2O_3$ was preliminarily determined by a chromatometric titration using exact amount of $K_2Cr_2O_7$. In all cases the end points were obtained using automatic titration apparatus (Akvilon ATP-02). The accuracy of the oxygen content determination was not less than ± 0.08.

Thermal expansion of ceramic samples versus temperature was measured with a high temperature dilatometer DIL 402 C Netzsch GmbH within the temperature range 298 – 1273 K in air with the heating/cooling rate 5 K/min. Dense ceramic samples of the $YBaCo_{2-x}Me_xO_{5+\delta}$ (Me=Fe, Cu) in the form of 2×2×15 mm bars for the thermal expansion measurements were obtained by pressing and sintering at 1323–1473 K in air for 15 h, with subsequent slow cooling (~1.5 K/min). The densities of the polished ceramic samples were not less than 90% of their theoretical values calculated from the XRD data. Similar samples were used for the electrical conductivity measurements using 4-probe DC technique.

Results and discussion

According to the results of XRD analysis (Fig.1a), the undoped $YBaCo_2O_{5+\delta}$ slowly cooled from 1373 K to room temperature is single phase with the layered perovskite-type structure. The value of oxygen content at 298 K in air, determined by TGA method is found equal to 5.41, which agrees with previous data [6, 19, 24]. The [110] and [001] ED patterns of this phase (Fig. 2b-c) and the corresponding [001] HRTEM image (Fig.2a) confirm that, at room temperature, it is tetragonal with the $3a_p \times 3a_p \times 2a_p$ supercell (S.G. *P4/mmm*), in agreement with the PXRD pattern. The tripling of the *a* parameter was previously explained by a 4:9 ordering of oxygen and vacancies located in the YO_δ layers, leading to the coexistence of cobalt ions with the octahedral (CoO_6) and pyramidal (CoO_5) coordination [6, 17, 25, 26]. The schematic model viewed along [001] is represented in Fig 2a as insert.

The study of the thermal stability of this phase in air shows that the [YO_δ] layers loose progressively oxygen as the temperature is increased, reaching the composition $YBaCo_2O_{5.06}$ at 1123 K (Table 1). The *in situ* high temperature X-ray diffraction study in the range 298–1123 K in air, shows that the tetragonal symmetry of the double perovskite, particularly the doubling of the *c* parameter is maintained in the whole temperature range. In contrast, the superstructure reflections corresponding to the tripling of the *a* parameter are too weak to be detected from the PXRD patterns and may possibly disappear as the temperature increases, i.e. as the oxygen stoichiometry approaches "O_5".

This viewpoint is strongly supported by TEM observations, where the reflections responsible for the tripling of the *a* parameter in the ED patterns of $YBaCo_2O_{5.41}$ (see Fig.2b,c), have disappeared after few minutes exposure to the electron beam inside of the microscope. This demonstrates that the latter heats the sample and allows topotactic oxygen departure without any destruction of the $YBaCo_2O_5$ framework, leading to the $a_p \times a_p \times 2a_p$ structure (S.G. *P4/mmm*). The latter indicates either a pure "O_5" composition or a very small deviation from this stoichiometry, with a statistical distribution of oxygen and vacancies in the YO_δ plane.

The unit cell parameters and volume, refined from XRD results for $YBaCo_2O_{5+\delta}$ at different temperatures, are listed in Table 1, keeping the tripling of the *a* parameter whatever the oxygen content for the sake of comparison. One observes that both lattice parameters increase with temperature due to the both physical and chemical expansion. Note that the oxygen content decreases as the temperature increases, leading to the continuous substitution of Co^{2+} for Co^{3+}.

The investigation of the $YBaCo_{2-x}Me_xO_{5+\delta}$ (Me=Fe, Cu, Ni) systems, in the range, $0.0 \leq x \leq 1.0$, in step of 0.1, according to the experimental conditions described above, allows single phase samples, with the layered perovskite type structure to be synthesized in air with a rather large homogeneity range, $0 \leq x \leq 0.7$ for Me=Fe and $0 \leq x \leq 0.6$ for Me=Cu, in agreement with the results previously reported for $YBaCo_{2-x}Me_xO_{5+\delta}$ [18,20]. In contrast, for Me =Ni, the solid solution exists only in a narrow compositional range $0.0 \leq x \leq 0.1$.

The oxygen content of these oxides determined by TGA and from chemical titration (Table 2) shows two important features:

(i) The introduction of the trivalent cation Fe^{3+} on the cobalt site increases the oxygen content with respect to the undoped cobaltate $YBaCo_2O_{5.41}$. Moreover, in the series $YBaCo_{2-x}Fe_xO_{5+\delta}$ the oxygen content (δ) increases with the iron content (x), tending toward a full occupancy of the oxygen sites of the perovskite ($O_{5.79}$ instead of O_6).

(ii) The introduction of the divalent cation Cu^{2+} on the cobalt site does the opposite. It decreases the oxygen content with respect to the undoped phase. Symmetrically, the oxygen content (δ) decreases as the copper content (*x*) increases, tending toward a complete disappearance of oxygen within the [YO_δ] layers ($O_{5.05}$ instead of O_5). Note that Ni is showing a similar tendency but its

very small homogeneity range suggests a different behaviour that will be discussed further.

The above observations raise the issue of the influence of the Fe/Cu substitution at cobalt site upon the oxygen ordering in the [YO_δ] layers of the undoped phase$YBaCo_2O_{5.41}$. The detailed structural study of the two limit compounds $YBaCo_{1.3}Fe_{0.7}O_{5.79}$ and $YBaCo_{1.4}Cu_{0.6}O_{5.05}$ answers this question. The electron microscopy study of these oxides clearly establishes that they both exhibit identical [010] and [001] ED patterns (Fig.3c-d) and corresponding HRTEM [001] images (Fig.3a), indicating the absence of superstructure in the *a,b* plane in contrast to the undoped phase, whereas the doubling of the *c* parameter is maintained (Fig.3b). The structural parameters of these two oxides (Table 3) determined from PXRD patterns (Fig. 1b-c) by Rietveld refinements in the $a_p \times a_p \times 2a_p$ (*P4/mmm*) structure and the corresponding ED patterns and HRTEM images for two main zone axis [001] and [100] (Fig.3a and b respectively) are in agreement with these observations.

The theoretical value of oxygen content that can lead to the ideal ordering of oxygen vacancies in $YBaCo_2O_{5+\delta}$ corresponding to the tripling of the cell parameters in the *a-b* planes is 5.44 [2,26]. In fact most of the known *Ln*$BaCo_2O_{5+\delta}$ (*Ln* = Pr - Gd) oxides can reach this value depending on the conditions (T, Po_2) [1, 10, 12-15, 27], however none of them have been reported to form $3a_p \times 3a_p \times 2a_p$ supercell. Thus, it can be suggested that, in the undoped cobaltate $YBa_2Co_2O_{5.41}$, there are some other factors (beside the exact 4 : 9 ratio of the vacancies and oxygen content) responsible for the formation of the supercell. The relatively high temperature, at which the other *Ln*$BaCo_2O_{5+\delta}$ phases reach the oxygen content equal to 5.44, where oxygen atoms can easily move within the [*Ln*O_δ] layers, probably prevents the formation of this ordered structure. Alternatively, random distributions of the dopant species that exhibit either donor or acceptor properties (even if the correct ratio of vacancies and oxygen atoms is maintained) can also disturb the possible ordering.

It is not the aim of this work to determine the critical Fe or Cu content that is necessary to destroy the particular oxygen ordering in $YBaCo_2O_{5.41}$. Nevertheless, it can be emphasized that, even for low copper contents in the oxides $YBaCo_{2-x}Cu_xO_{5+\delta}$, i.e. x=0.2, the TEM investigation shows the complete absence of superstructure reflections in the *a,b* plane, whereas the doubling of the *c* parameter is maintained. In contrast, for the same Fe content, x=0.2, the oxide $YBaCo_{2-x}Fe_xO_{5+\delta}$ still exhibits a tripling of its *a=b* parameter from ED patterns. Thus the structure of the Fe-doped phase (Fig.4a) can be described as an oxygen

deficient octahedral framework, with the oxygen vacancies distributed at random in the [YO] layers, whereas the Cu-doped phase (Fig.4b) can be represented as a pyramidal framework, with excess oxygen distributed at random in the [Y] layers. Quite remarkably, the Ni-doped cobaltate $YBaCo_{1.9}Ni_{0.1}O_{5.32}$ shows also the absence of superstructure in the *a,b* plane from its ED patterns, in spite of its low doping level at the Co site. Thus, this demonstrates that the $3a_p \times 3a_p \times 2a_p$ superstructure is extremely sensitive to the doping of the cobalt sites and that the oxygen/ vacancy ordering in the (001) plane is easily destroyed by this doping, whatever the nature of the dopant, leading to the $a_p \times a_p \times 2a_p$ structure.

The substitution of iron or copper for cobalt leads to a monotonous increase of the unit cell parameters and of the unit cell volumes with *x* (Fig. 5). This behavior is different from that of the oxygen content for these two species which varies in opposite directions for Fe and Cu (Fig.6), leading to an increase of the average oxidation state of the 3d-transition metal to values higher than +3 for Fe and to a decrease to values smaller than +3 for Cu. In fact, this demonstrates that the size of the transition metal cation is playing the major role in this evolution. Indeed, the ionic radii of iron ($r_{Fe^{3+}/Fe^{4+}}$ = 0.785/0.725 Å, CN=6) and copper ($r_{Cu^{2+}/Cu^{3+}}$ = 0.87 / 0.68 Å, CN=6) are larger than those of cobalt ($r_{Co^{3+}/Co^{4+}}$ = 0.75/0.67 Å, CN=6) [28]. Similar results have been reported in the Fe-doped $LnBaCo_2O_{5+\delta}$ (Ln=Nd, Sm, Gd, Ho) systems [10-14, 18, 29].

This opposite ability of iron to increase the oxygen content and of copper or nickel to decrease it can be explained by the fact that iron is a more electropositive element in comparison to cobalt and therefore acts as a donor of electrons ($Fe_{Co}^{\bullet}$) that retains oxygen in the lattice and prevents the formation of oxygen vacancies ($V_O^{\bullet\bullet}$). On the contrary, Cu-substitution promotes oxygen desorption and formation of oxygen vacancies ($V_O^{\bullet\bullet}$) since it acts as an acceptor of electrons ($Cu_{Co}^{/}$). The same tendency was observed for the perovskite-type oxides $La_{1-x}Sr_xCo_{1-y}Me_yO_{3-\delta}$ (Me=Fe, Ni) [30]. A similar behavior should be expected for the Ni-doped oxide, but the difficulty of Ni^{2+} to accommodate the pyramidal coordination most probably limits its homogeneity range to x=0.1.

The PXRD study of the thermal stability of the oxides in air up to 1273 K shows that they keep their structure in the whole temperature range. This is exemplified for the high temperature XRD patterns which all exhibit the tetragonal $a_p \times a_p \times 2a_p$ (S.G. *P4/mmm*) structure within the temperature range studied.

The values of the oxygen content in the $YBaCo_{2-x}Me_xO_{5+\delta}$ (Me=Fe, Cu, Ni) as a function of temperature are shown in Fig. 7. Each experimental curve $(5+\delta) - f(T)$ can be divided into three parts. The values of oxygen content remain practically unchanged from room temperature to approximately 600 K, presumably due to a kinetics reason. Significant loss of oxygen for all the samples is observed within the temperature range starting from ~ 600 K up to 830 - 955 K. Further increase of temperature leads to the appearance of inflection for the curves and reveals saturation tendency. As can be seen from the Fig. 7, Fe for Co substitution increases the oxygen content while Ni and Cu decrease it. Such behavior was explained above. As a result, the mean oxidation state of the 3d-transition metals increases in the Fe-doped oxides and decreases in the Ni- and Cu-doped phases (Fig. 6, Tables 4,5). Since the substitution of Cu or Ni for Co leads to a significant decrease of oxygen content (at fixed T and Po_2) it could be concluded that the dopant species adopt the Me^{2+} state rather than Me^{3+} and provoke the formation of oxygen vacancies ($V_O^{\bullet\bullet}$) in equivalent amounts. Also, considering the red-ox equation $Co^{3+} + Me^{2+} = Me^{3+} + Co^{2+}$ for Me = Cu, Ni in the $YBaCo_{2-x}Me_xO_{5+\delta}$ oxides one can assume that Cu^{2+} and Ni^{2+} are more stable, compared to Cu^{3+} and Ni^{3+}. Then, it is possible to estimate the average oxidation state of cobalt (Table 4). The obtained results show that when the oxygen content is far enough from the "O_5" value, irrespective of the nature and concentration of dopant (Ni, Cu), the average valence of cobalt remains practically unchanged, around +2.8. In contrast, since at room temperature the values of oxygen content in Fe-substituted solid solutions are larger than 5.5, the mean oxidation state of 3d-transition metals is higher that 3+. Since cobalt is the more electronegative element it is possible to assume that all cobalt ions are in a Co^{3+} state meanwhile iron is responsible for the appearance of 4+ state. This approach allowed calculating Fe^{4+} content and its fraction $\left(\frac{Fe^{4+}}{x}\right)$ (Table 5). One observes that the Fe^{4+} fraction increases with the iron content.

Another noticeable feature that deserves attention is the high temperature inflection point in the dependence of oxygen content versus temperature. Whereas such inflection points for the Ni- and Cu-substituted solid solutions, and even for undoped $YBaCo_2O_{5+\delta}$ can be treated as a change of oxygen content towards "O_5", the significant increase of $(5+\delta)$ value in the inflection point for the Fe-substituted oxides is not so clear. Since in all the Fe-samples, the oxygen content at the highest measured temperature (about 1325 K) is smaller that 5.5, one should conclude that the oxidation states of the 3d-transition metals are distributed

between 2+ and 3+. Assuming that more electropositive iron reveals the only oxidation state equal 3+, the content of cobalt in Co^{2+} and Co^{3+} forms can be estimated (Table 6). The continuous increase of the cobalt oxidation state reflects the influence of the increase of iron content since the latter retains oxygen in the lattice more strongly than cobalt. Another interesting point is the decrease of the percentage of Co^{2+} ions. Such a reduction in Co^{2+} ions content down to zero may prevent further substitution of Fe for Co in the $YBaCo_{2-x}Fe_xO_{5+\delta}$ series. Indeed, further increase of the average oxidation state for cobalt and iron (at these conditions T, Po_2) is unfavorable, and can explain the substitution limit that was found between x=0.7 and 0.8.

The temperature dependence of the electrical conductivity (Fig.8) shows that all the oxides $YBaCo_{2-x}Me_xO_{5+\delta}$ exhibit a maximum of the conductivity at approximately 600 K. It was shown earlier that the most mobile charge carriers in the rare earth and barium cobaltates with the double perovskites structure are electronic holes and that the conductivity can be described by small polaron mechanism [10,17,18, 31]. Within the model suggested by Tsvetkov et al. [31] there are three main processes that are determining the defect structure:

$$O_O^{\times} + 2Co_{Co}^{\bullet} = \frac{1}{2}O_2 + V_O^{\bullet\bullet} + 2Co_{Co}^{\times} \quad (1)$$

$$2Co_{Co}^{\times} \Leftrightarrow Co'_{Co} + Co_{Co}^{\bullet} \quad (2)$$

$$V_O^{\bullet\bullet} + Ba'_{Gd} \Leftrightarrow (V_O^{\bullet\bullet} - Ba'_{Gd})^{\bullet} \quad (3)$$

According to this model, the fact the conductivity rises from room temperature to 600 K (Fig.8), while the oxygen exchange is negligible (Fig.7), can be explained by the intrinsic charge disproportionation (reaction (2)). Further increase of temperature leads to a significant increase of oxygen vacancies $[V_O^{\bullet\bullet}]$ and hence the concentration of the most mobile electronic holes $[Co_{Co}^{\bullet}]$ decreases according to reaction (1).

Introduction of iron leads to a significant decrease of conductivity since it acts as an hole trap $Fe_{Co}^{\bullet}$. Small addition of the acceptor type dopant (Ni'_{Co}, x=0.1) yields an increase of mobile charge carriers according to the reaction:

$$Co_{Co}^{\times} + Ni_{Co}^{\times} \Leftrightarrow Co_{Co}^{\bullet} + Ni'_{Co} \quad (4)$$

and hence, one observes a significant increase of the conductivity (Fig. 8). However further increase of the acceptor dopant content decreases the number of available sites for charge

carrier hopping and also promotes the formation of oxygen vacancies according to the reaction:

$$O_O^{\times} + 2Cu_{Co}^{\times} = \frac{1}{2}O_2 + V_O^{\bullet\bullet} + 2Cu'_{Co} \qquad (5)$$

that breaks the migration path ($Me^{\bullet} - O - Me^{\times}$ or $Me' - O - Me^{\times}$) and therefore results in a decrease of the conductivity value for $YBaCo_{1.6}Cu_{0.4}O_{5+\delta}$ in comparison with the undoped sample. The slight increase of conductivity with temperature for $YBaCo_{1.6}Cu_{0.4}O_{5+\delta}$ at approximately 800 K (Fig. 8) coincides with the plateau on the temperature dependence of oxygen content for this oxide (Fig.7). Although the mobility of electrons Me'_{Co} is smaller in comparison with the holes [29] their concentration becomes much larger when the oxygen content tends toward 5. This was observed even in the undoped gadolinium/barium cobaltate [32]. Therefore, one can suppose that at some point, electrons start to play a significant role in the charge transfer, especially in the acceptor doped $YBaCo_{1.6}Cu_{0.4}O_{5+\delta}$. Moreover, even if the concentration of electronic charge carriers (electrons and holes) remains unchanged their mobility increases with temperature [32] and consequently the value of the total conductivity is increased.

The thermal expansion behavior of the $YBaCo_{2-x}Me_xO_{5+\delta}$ (Me=Fe, Cu, Ni) ceramics is illustrated in Fig. 9. The quasi-linearity of the curves $\Delta L/L=f(T)$ proves the absence of phase transition within the studied temperature range in good agreement with the results of high temperature XRD. The thermal expansion dependence was linearly fitted in the temperature range 298–1273K. The calculated thermal expansion coefficients (TECs) in the investigated temperature range are listed in Table7.

The volumetric thermal expansion coefficients for two samples $YBaCo_{2-x}Cu_xO_{5+\delta}$ (x=0, 0.4) were obtained using high temperature XRD data and then with the adjustment for the density of ceramic samples they were recalculated to the linear thermal expansion coefficients. These results within the error are in good agreement with the dilatometry data in this temperature range (Table 7).

Although the difference between the TEC values for the studied solid solutions and electrolyte materials ($Ce_{0.8}Sm_{0.2}O_{2-\delta}$ and $Zr_{0.85}Y_{0.15}O_{2-\delta}$) for the solid oxide fuel cells are rather large they still can be used in the form of composite materials. In this respect, the absence of chemical reactivity between $YBaCo_{2-x}Me_xO_{5+\delta}$ (Me=Fe, Cu, Ni) and electrolyte materials plays an important role. In order to check possible chemical interactions, the

$YBaCo_{2-x}Me_xO_{5+\delta}$ (Me=Fe, Cu; x=0.0; 0.4; 0.6) samples were mixed with solid electrolyte materials, namely $Ce_{0.8}Sm_{0.2}O_{2-\delta}$ and $Zr_{0.85}Y_{0.15}O_{2-\delta}$ in the mass ratio 1 : 1 and fired during 20 hours at 1073 K, 1173 K, 1273 K and 1373 K in air. It was found that $YBaCo_{2-x}Me_xO_{5+\delta}$ with Me = Fe (x = 0.4) and Cu were chemically inert to the $Ce_{0.8}Sm_{0.2}O_{\delta-2}$ in the temperature range 1073 – 1273 K, while $YBaCo_{1.4}Fe_{0.6}O_{5+\delta}$ was chemically inert to the $Ce_{0.8}Sm_{0.2}O_{2-\delta}$ within all the studied temperature range. In contrast, $Zr_{0.85}Y_{0.15}O_{2-\delta}$ even at 1173 K noticeably reacts with $YBaCo_{2-x}Me_xO_{5+\delta}$ (Me=Fe, Cu; x=0.0; 0.4; 0.6) forming the highly resistive phase $BaZrO_3$. The XRD patterns of the $YBaCo_{2-x}Fe_xO_{5+\delta}$ (x=0; 0.6) + $Ce_{0.8}Sm_{0.2}O_{2-\delta}$ and $YBaCo_2O_{5+\delta}$ + $Zr_{0.85}Y_{0.15}O_{2-\delta}$ at T=1073 K and 1173 K mixtures are shown in Figs. 10 and 11.

Conclusion

This study of the oxides $YBaCo_{2-x}Me_xO_{5+\delta}$, with Me=Fe, Ni, Cu, shows that it is possible to tune the oxygen content in these layered "112" perovskites by substituting a 3d-transition element for cobalt. In these substituted oxides the 1:1 ordering between the Ba and Y layers is maintained, whereas the ordering of oxygen and vacancies in the YO_δ layers is destroyed, leading to an $a_p \times a_p \times 2a_p$ structure. Importantly the chemical nature of the transition metal dopant has a specific role. For a donor type Fe-substituted oxide the oxygen content is larger than for the undoped phase and increases with the substitution level, tending toward the pure octahedral $YBaCo_{2-x}Fe_xO_6$ double perovskite. In contrast, for a divalent cation like Cu^{2+} the oxygen content is smaller and decreases as the substitution level increases, tending toward the pure pyramidal $YBaCo_{2-x}Cu_xO_5$ phase. This different behavior can be explained on the basis of the more electropositive character of Fe compared to Cu. In the case of nickel substitution, the very small substitution range that is obtained is explained by the fact that Ni^{2+}, contrary to the Jahn-Teller cation Cu^{2+} does not accommodate easily the pyramidal coordination. Possible variations of the oxidation states for the Co and Fe ions within the temperature have been discussed.

The evolution of the conductivity of these substituted oxides versus temperature is closely related to the loss of oxygen and can be explained on the basis of a defect model previously suggested by Tsvetkov et al. [29].

The thermal expansion shows the absence of phase transition in all complex oxides within the studied temperature range**.** The study of the chemical compatibility of these oxides with the two electrolyte materials $Zr_{0.85}Y_{0.15}O_{2-\delta}$ and $Ce_{0.8}Sm_{0.2}O_2$ shows that one of them,

$YBaCo_{1.4}Fe_{0.6}O_{5+\delta}$, does not exhibit interaction with the $Ce_{0.8}Sm_{0.2}O_{2-\delta}$ electrolyte, suggesting the possibility of application.

These results, which demonstrate the possibility to tune the oxygen content in the layered 112 cobaltates open the route to the systematic exploration of this family, and also should be transposed to other oxygen deficient perovskite derivatives in view of the realization of solid oxide fuel cells.

Acknowledgments

This work was financially supported in parts by the Russian Foundation for Basic Research (Project No 13-03-00958) and by the Ural Federal University development program for young scientists.

References

[1] J.-H. Kim and A. Manthiram, *J. Electrochem. Soc,* 2008, **155,** 385-390.

[2] Y. Liu, *J. Alloys and Compounds*, 2009, **477**, 860–862.

[3] K. Zhang, L. Ge, R. Ran, Z. Shao and S. Liu, *Acta Materialia*, 2008, **56**, 4876-4889.

[4] L. Barbey, N. Nguyen, V. Caignaert, F. Studer, B. Raveau, *J. Solid State Chem*., 112 (1994) 148-156.

[5] Cobalt Oxides. From Crystal Chemistry to Physics. by B. Raveau and M. Seikh, Wiley-VCH Verlag GmbH & Co. KGaA, Weinheim, 2012.

[6] D. Akahoshi, Y. Ueda, *J. Solid State Chem*., 2001, **156**, 355-363.

[7] G. Aurelio, J. Curiale, R.D. Sanchez, *Physica B*, 2006, **384**, 106-109.

[8] L. Er-Rakho, C. Michel and B. Raveau, *J. Solid State Chem*., 1988, **73**, 531-535.

[9] J.-H. Kim, A. Manthiram, *Electrochim. Acta*, 2009, **54**, 7551-7557.

[10] N.E. Volkova, L.Ya. Gavrilova, V.A. Cherepanov, T.V. Aksenova, V.A. Kolotygin and V.V. Kharton, *J. Solid State Chem.*, 2013, **204**, 219-223.

[11] L.Ya. Gavrilova, N.E. Volkova, T.V. Aksenova and V.A. Cherepanov, *Mat. Res. Bull.*, 2013, **48**, 2040-2043.

[12] V.A. Cherepanov, T.V. Aksenova, L.Ya. Gavrilova and K.N Mikhaleva, *Solid State Ionics*, 2011, **188**, 53-57.

[13] D.S. Tsvetkov, I.L. Ivanov and A.Yu. Zuev, *J. Solid State Chem*., 2013, **199**, 154-159.

[14] D.S. Tsvetkov, I.L. Ivanov and A.Yu. Zuev, *Solid State Ionics,* 2012, **218**, 13-17.

[15] A.Yu.Suntsov, I.A.Leonidov, M.V.Patrakeev and V.L.Kozhevnikov, *J. Solid State Chem,* 2013, **206**, 99–103.

[16] Seonyoung Yoo, Jee Young Shin and Guntae, *J. Electrochem. Soc.*, 2011, **158,** B632-B638.

[17] W. Zhou, *Chem. Mater*. 1994, **6**, 441-447.

[18] X. Zhang, H. Hao, Q. He and X. Hu*, Physica B*, 2007, **394**, 118-121.

[19] V.A. Cherepanov, L.Ya. Gavrilova, T.V. Aksenova, A.S. Podzorova, N.E. Volkova and E.V. Plotnikova, *MRS Online Proceedings Library*, 2012, **1384**, mrsf11-1384-b14-04.

[20] J. Xue, Y. Shen and T. He, *J. Power Sources,* 2011, **196,** 3729–3735.

[21] X. Zhang, H. Hao and X. Hu, *Physica B*, 2008, **403**, 3406-3409.

[22] V.K. Pecharsky and P.Y. Zavalij, Fundamentals of Powder Diffraction and Structural Characterization of Materials, second ed., Springer, New York, 2005.

[23] R.E. Dinnebier and S.J.L. Billinge, Powder Diffraction. Theory and Practice, RSC Publishing, Cambridge, 2008.

[24] A.S. Urusova, V.A. Cherepanov, T.V. Aksenova, L.Ya. Gavrilova and E.A. Kiselev, *J. Solid State Chem*., 2013, **202**, 207-214.

[25] D.D. Khalyavin, D.N. Argyriou, U. Amann, A.A. Yaremchenko and V.V. Kharton,*Phys. Rev. B,* 2007, **75**, 134407-134422

[26] W. Zhou, C.T. Lin and W.Y. Liang, *Adv. Mater.*, 1993, **5**, 735-738.

[27] T.V. Aksenova, L.Ya. Gavrilova, D.S. Tsvetkov, V.I. Voronin and V.A. Cherepanov, *Russ. J. Phys. Chem. A,* 2011, **85**, 427–432.

[28] R.D. Shannon, *Acta Cryst*., 1976, **32**, 751–767.

[29] D.S. Tsvetkov, I.L. Ivanov and A.Yu. Zuev, *J. Solid State Chem*., 2013, **199**, 154-159.

[30] V. Cherepanov, T. Aksenova, E. Kiselev and L. Gavrilova, *Solid State Sciences*, 2008, **10**, 438–443.

[31] D.S. Tsvetkov, V.V. Sereda and A.Yu. Zuev, *Solid State Ionics*, 2011, **192**, 215–219.

[32] D.S. Tsvetkov, V.V. Sereda and A.Yu. Zuev, *Solid State Ionics*, 2010, **180**, 1620–1625.

Figure captions

Figure 1. Rietveld refinement profiles of the slowly cooled $YBaCo_2O_{5+\delta}$ (a), $YBaCo_{1.3}Fe_{0.7}O_{5+\delta}$ (b) and $YBaCo_{1.4}Cu_{0.6}O_{5+\delta}$ (c) at room temperature in air.

Figure 2. (a), (d) - Bright field HRTEM image along the [001] zone axis of $YBaCo_2O_{5.41}$ structure. (b), (c) - ED pattern taken along [001] and [110] zone axis correspondingly. Tripling of a_p is clearly visible. (d) – enlargement of HRTEM image rectangle area selected with in (a) showing pronounced $3a_p x 3a_p$ superstructure. The corresponding structural model of ordering in [001] plane is given as insert where (Ba,Y) columns are blue, Co is yellow.

Figure 3. Bright field HRTEM image along [001] – (a) and [010] – (b) zone axis of $YBaCo_{2-x}Me_xO_{5+\delta}$ (Me=Fe, Cu,) (x=0.2-0.7) structures and corresponding ED patterns. No superstructure spots are visible in ED patterns. The corresponding structural models are given as insert where Y is red Ba is blue, Co is yellow.

Figure 4. Schematic presentation of the 112 structure with oxygen octahedral framework corresponding to the $LnBaMeO_6$ (a) and oxygen pyramidal framework corresponding to the $LnBaMeO_5$ (b).

Figure 5. The unit cell parameters and volumes for the $YBaCo_{2-x}Me_xO_{5+\delta}$ versus composition of solid solution: Me=Fe (a) and Cu (b).

Figure 6. Dependence of the oxygen content and mean oxidation state of 3d transition metal (n) in the $YBaCo_{2-x}Me_xO_{5+\delta}$ Me = Fe and Cu versus 3*d*-metal dopant content at room temperature.

Figure 7. Variation of the oxygen content versus temperature in $YBaCo_{2-x}Me_xO_{5+\delta}$ in air: Me=Fe (a) and Cu, Ni (b).

Figure 8. Dependence of the electrical conductivity versus temperature for the $YBaCo_{2-x}M_xO_{5+\delta}$ (Me = Fe, Ni, Cu) solid solutions.

Figure 9. Linear thermal expansion of the $YBaCo_{2-x}M_xO_{5+\delta}$ (M=Fe, Cu) ceramics in air: (a) 298–1273 K; (b) 1213–1268 K.

Figure 10. Chemical compatibility of the $YBaCo_{2-x}Fe_xO_{5+\delta}$ (x=0; 0.6) with electrolyte material $Ce_{0.8}Sm_{0.2}O_{2-\delta}$ (T=1373 K and Po_2=0.21 atm.).

Figure 11. Chemical compatibility of the $YBaCo_2O_{5+\delta}$ with electrolyte material $Zr_{0.85}Y_{0.15}O_{2-\delta}$ (T=1073 K, 1173 K and Po_2=0.21 atm.).

Table 1.Unit cell parameters, unit cell volume and oxygen content of $YBaCo_2O_{5+\delta}$ at temperatures 298 –1123 K in air

T, K	*a*, Å	*c,* Å	*V,* (Å)^3	Refinement parameters			Oxygen content (5+δ)
				$R_{Br,}$%	$R_{f,}$%	$R_{p,}$%	
298	11.629(1)	7.503(1)	1014.75(3)	1.34	2.03	8.80	5.41*
							5.40**
673	11.703(1)	7.567 (1)	1036.45(1)	2.04	3.14	12.50	5.32*
873	11.750(1)	7.585(1)	1047.31(1)	1.66	3.06	10.90	5.14*
923	11.762(2)	7.592(0)	1050.31(0)	1.53	3.27	12.60	5.11*
973	11.771(0)	7.601(2)	1053.17(2)	2.32	3.73	9.72	5.09*
1023	11.782(1)	7.611(1)	1056.53(1)	2.14	2.35	10.40	5.08*
1073	11.791(1)	7.617 (1)	1059.01(2)	2.17	2.58	12.20	5.06*
1123	11.801(1)	7.624(2)	1061.75(2)	2.27	3.19	11.20	5.06*

* data obtained by TGA
** data obtained by titration

Table 2. Cell parameters and volumes refined by the Rietveld analysis and values of oxygen content for the $YBaCo_{2-x}Me_xO_{5+\delta}$ solid solutions

Me	*X*	*a*, Å	*c,* Å	*V,* (Å)^3	Refinementparameters			Oxygen content (5+δ)
					$R_{Br,}$ %	$R_{f,}$ %	$R_{p,}$ %	
-	0.0	11.629(1)	7.503(1)	1014.75(3)	1.34	2.03	8.80	5.41*
Fe	0.2	11.630(1)	7.511(1)	1016.1(1)	2.17	2.30%	12.9%	5.53*
	0.4	3.880(1)	7.528(1)	113.33(1)	1.56%	2.20%	6.78%	5.64*
	0.6	3.882(0)	7.544(2)	113.69(4)	1.97%	2.24%	12.5%	5.74*
	0.7	3.883(1)	7.558(0)	113.96(2)	2.06%	3.59%	12.4%	5.79*
Cu	0.2	3.874(1)	7.509(1)	1014.1(1)	1.99%	3.41%	12.4%	5.26**
	0.4	3.877(0)	7.519(1)	113.02(1)	1.94%	2.60%	11.6%	5.19**
	0.6	3.878(1)	7.528(1)	113.21(2)	1.70%	3.13%	10.6%	5.05**
Ni	0.1	3.876(0)	7.496(1)	112.62(1)	2.21%	2.60%	6.90%	5.32**

* data obtained by TGA
**data obtained by titration

Table 3. The structural parameters and *R*-factors refined by the Rietveld method for the $YBaCo_{2-x}M_xO_{5+\delta}$ solid solutions

P4/mmm space group, Y(1d) (0.5; 0.5; 0.5), Ba(1c) (0.5; 0.5; 0), Co/Fe/Cu(2g) (0;0;*z*), O1(1a) (0;0;0), O2(1b) (0;0;0.5), O3(4i) (0;0.5;*z*)*		
	$YBaCo_{1.3}Fe_{0.7}O_{5+\delta}$	$YBaCo_{1.4}Cu_{0.6}O_{5+\delta}$
a, Å	3.883(1)	3.878(1)
c, Å	7.558(1)	7.528(1)
V, $(Å)^3$	114.01(1)	113.198(1)
z(Co/Fe/Cu)	0.258(1)	0.270(1)
z(O3)	0.305(1)	0.316(1)
Occ.	0.377(1)	0.107(1)
$d_{Y\text{-}Co}$, Å	3.298(1)	3.262(1)
$d_{Y\text{-}O3}$, Å	2.493(1)	2.383(1)
$d_{Ba\text{-}Co}$, Å	3.369(1)	3.388(1)
$d_{Ba\text{-}O3}$, Å	2.946(1)	3.069(1)
$d_{Co\text{-}O1}$, Å	1.953(1)	1.998(1)
$d_{Co\text{-}O2}$, Å	1.827(1)	1.760(1)
$d_{Co\text{-}O3}$, Å	1.959(1)	1.969(1)
R_{Br}, %	2.06	2.24
R_f, %	3.59	4.01
R_p, %	12.4	11.43

* Oxygen atoms labeled as O1 correspond to the oxygen in BaO planes, those labeled as O2 correspond to the oxygen in YO_δ planes (thus, the occupancy factor found is given), and those labeled as O3 correspond to the oxygen in CoO_2 planes.

Table 4. Calculated values of the oxidation states of cobalt in $YBaCo_{2-x}Me_xO_{5+\delta}$ (Me= Cu, Ni) oxides at room temperature

x	(5+δ)	Mean oxidation state of 3d-metal	Oxidation state of Co
Me = Ni			
0.1	5.32	2.82	2.86*
Me = Cu			
0.2	5.26	2.76	2.84*
0.4	5.19	2.69	2.86*
0.6	5.05	2.55	2.79*

* in the assumption that all nickel and copper is in Me^{2+} form

Table 5. Calculated values of the oxidation states of iron and fraction of Fe^{4+} in $YBaCo_{2-x}Fe_xO_{5+\delta}$ at room temperature

x	Fe^{3+} ions content	Fe^{4+} ions content	Fraction of Fe^{4+} ions $\frac{Fe^{4+}}{x}$,%
0.2	0.14*	0.06*	30
0.4	0.12*	0.28*	70
0.6	0.12*	0.48*	80
0.7	0.12*	0.58*	83

* in the assumption that all cobalt is in Co^{3+} form

Table 6. Calculated values of the oxidation states of cobalt and fraction of Co^{2+} in the $YBaCo_{2-x}Fe_xO_{5+\delta}$ at 1325 K.

x	(5+δ) at 1325 K	Oxidation state of Co ions	Co^{3+} ions content	Co^{2+} ions content	Fraction of Co^{2+} ions $\frac{Co^{2+}}{2-x}$, %
0	5.04	2.54*	1.08	0.92	46
0.2	5.17	2.63*	1.14	0.66	36.6
0.4	5.27	2.71*	1.14	0.46	28.75
0.6	5.38	2.83*	1.16	0.24	17.1
0.7	5.48	2.97*	1.26	0.04	3.1

* in the assumption that all iron is in Fe^{3+} form

Table 7. Average thermal expansion coefficients (TECs) of the $YBaCo_{2-x}Me_xO_{5+\delta}$ oxides in air

Me	*x*	ΔT, K	TEC×10^6, K^{-1}
	0.0	298–530	12.5
		530–1273	13.6
			14.5*
Fe	0.4	298–1273	15.1
Cu	0.4	298–1273	17.3
			16.1*
Ni	0.1	298–1273	18.8

* - calculated from the XRD data at high temperature

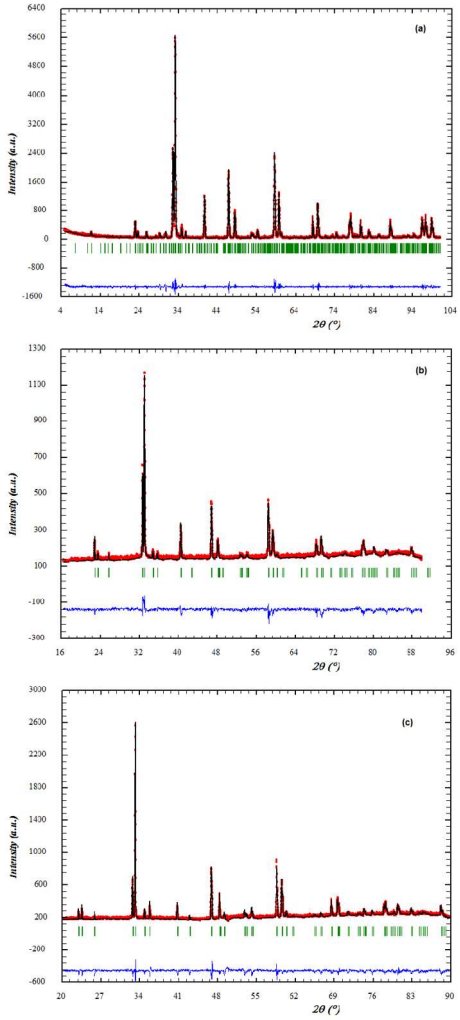

Figure 1

Rietveld refinement profiles of the slowly cooled $YBaCo_2O_{5+\delta}$ (a), $YBaCo_{1.3}Fe_{0.7}O_{5+\delta}$ (b) and $YBaCo_{1.4}Cu_{0.6}O_{5+\delta}$ (c) at room temperature in air.
236x562mm (96 x 96 DPI)

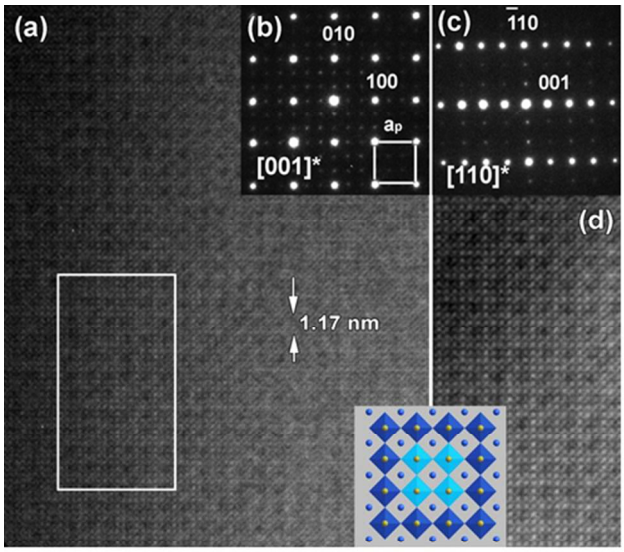

Figure 2

(a), (d) -Bright field HRTEM image along the [001] zone axis of $YBaCo_2O_{5.41}$ structure. (b), (c) - ED pattern taken along [001] and [110] zone axis correspondingly. Tripling of a_p *is clearly visible. (d) – enlargement of HRTEM* image rectangle area selected with in (a) showing pronounced $3a_p x 3a_p$ superstructure. The corresponding structural model of ordering in [001] plane is given as insert where (Ba,Y) columns are blue, Co is yellow. 211x158mm (96 x 96 DPI)

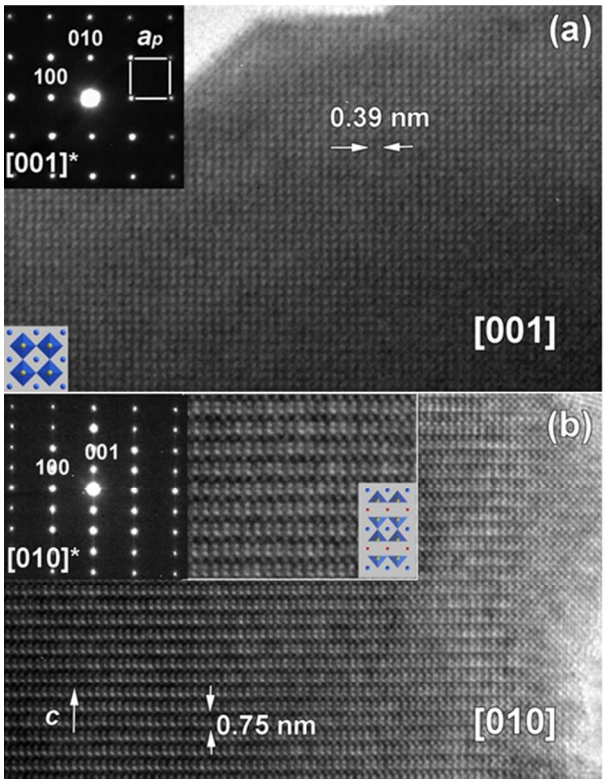

Figure 3

Bright field HRTEM image along [001] –(a) and [010] – (b) zone axis of $YBaCo_{2-x}Me_xO_{5+\delta}$ (Me=Fe, Cu,) (x=0.2-0.7) structures and corresponding ED patterns. No superstructure spots are visible in ED patterns. The corresponding structural models are given as insert where Y is red Ba is blue, Co is yellow.
211x163mm (96 x 96 DPI)

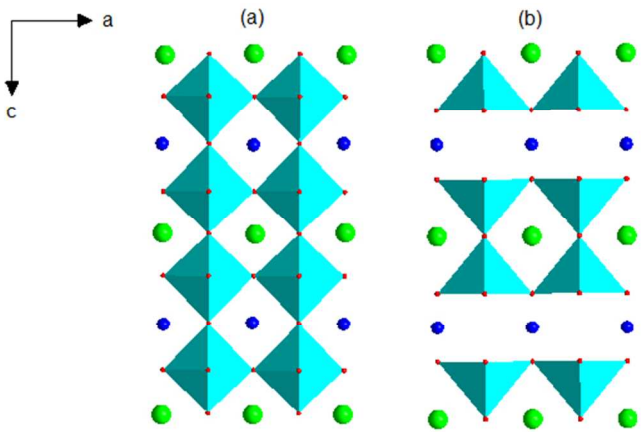

Figure 4

Schematic presentation of the 112 structure with oxygen octahedral framework corresponding to the LnBaMeO6 (a) and oxygen pyramidal framework corresponding to the LnBaMeO5 (b)
211x158mm (96 x 96 DPI)

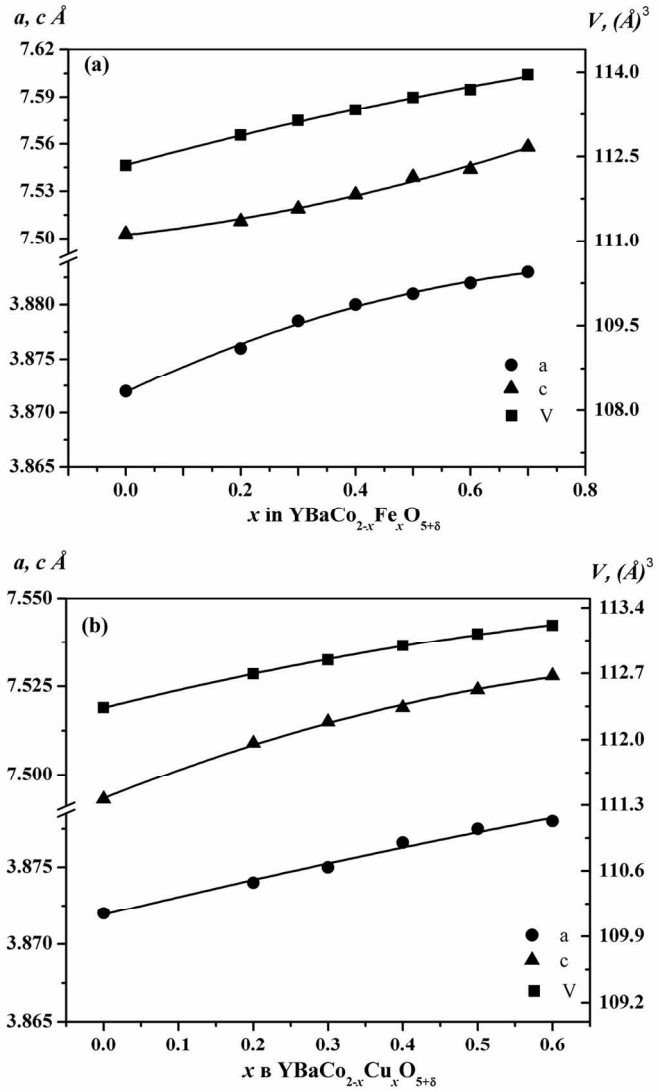

Figure 5

The unit cell parameters and volumes for the $YBaCo_{2-x}Me_xO_{5+\delta}$ versus composition of solid solution: Me=Fe (a) and Cu (b).
209x332mm (150 x 150 DPI)

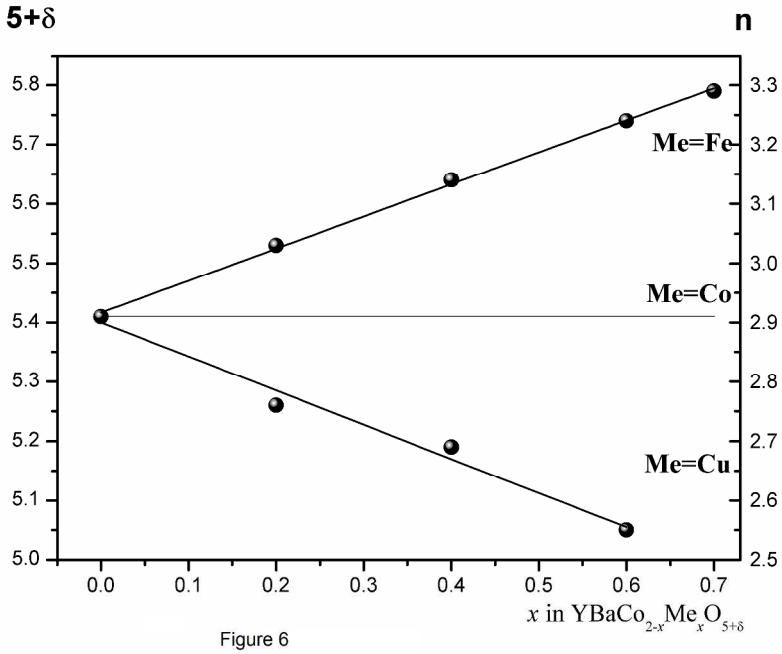

Figure 6

Dependence of the oxygen content and mean oxidation state of 3d transition metal (n) in the $YBaCo_{2-x}Me_xO_{5+\delta}$ Me = Fe and Cu versus 3d-metal dopant content at room temperature.
289x203mm (300 x 300 DPI)

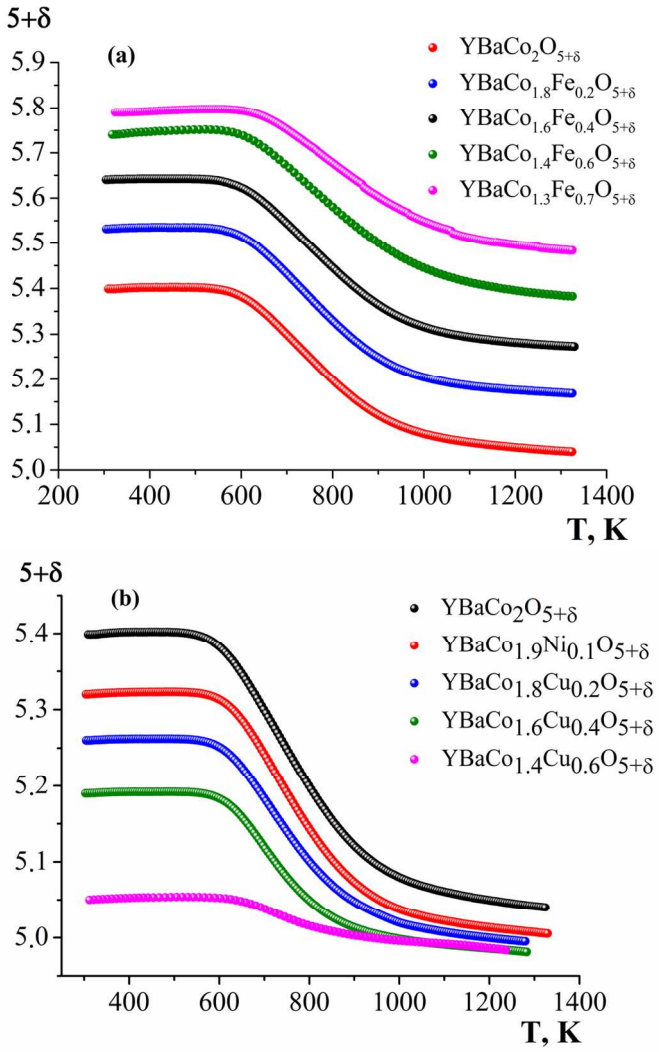

Figure 7

Variation of the oxygen content versus temperature in $YBaCo_{2-x}Me_xO_{5+\delta}$ in air: Me=Fe (a) and Cu, Ni (b).
209x340mm (150 x 150 DPI)

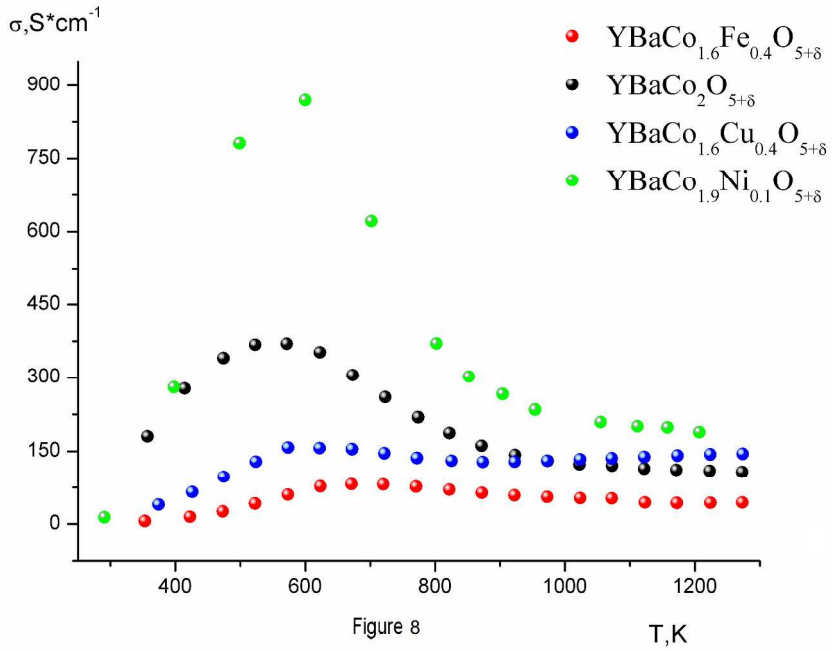

Dependence of the electrical conductivity versus temperature for the $YBaCo_{2-x}M_xO_{5+\delta}$ (Me = Fe, Ni, Cu) solid solutions.
289x201mm (300 x 300 DPI)

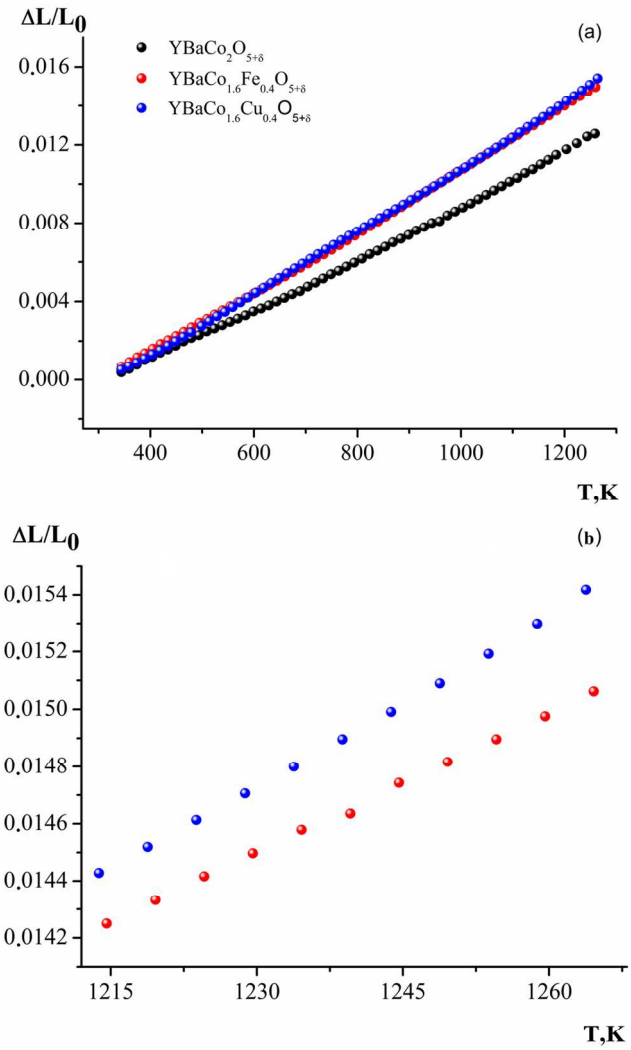

Figure 9

Linear thermal expansion of the $YBaCo_{2-x}M_xO_{5+\delta}$ (M=Fe, Cu) ceramics in air: (a) 298–1273 K; (b) 1213–1268 K.
209x340mm (150 x 150 DPI)

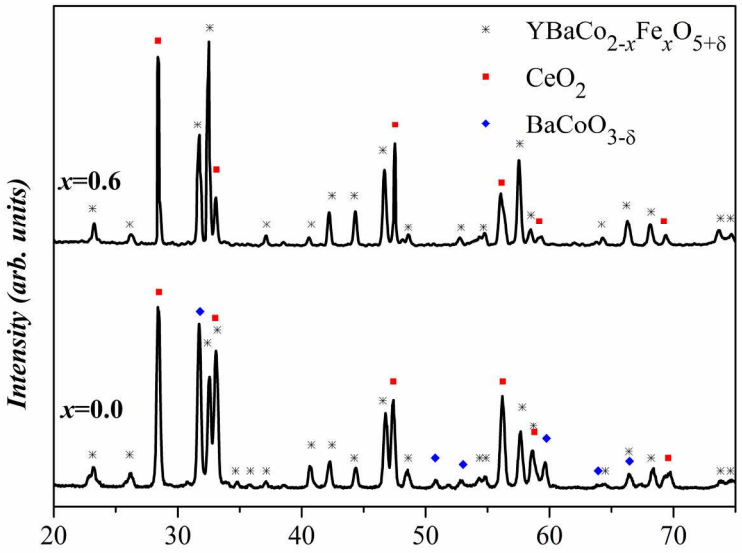

Figure 10

Chemical compatibility of the $YBaCo_{2-x}Fe_xO_{5+\delta}$ (x=0; 0.6) with electrolyte material $Ce_{0.8}Sm_{0.2}O_{2-\delta}$ (T=1373 K and Po2=0.21 atm.).
201x140mm (300 x 300 DPI)

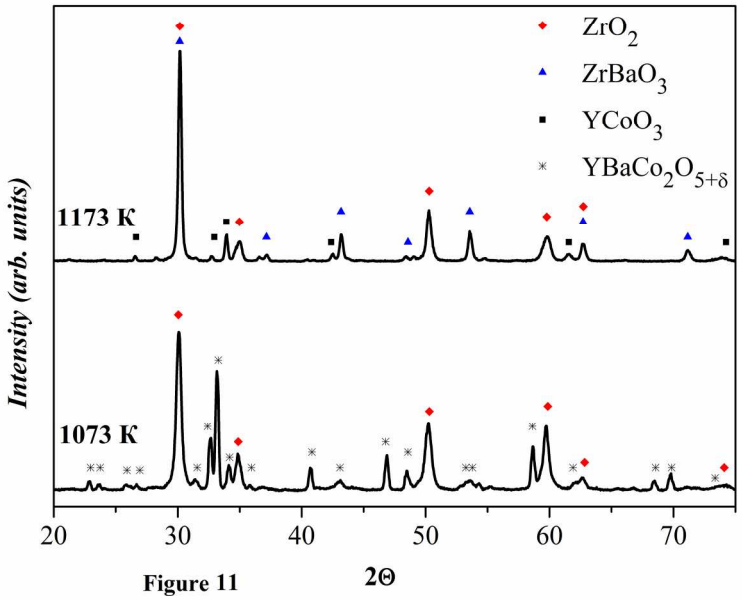

Figure 11

Chemical compatibility of the $YBaCo_2O_{5+\delta}$ with electrolyte material $Zr_{0.85}Y_{0.15}O_{2-\delta}$ (T=1073 K, 1173 K and Po2=0.21 atm.).
201x140mm (300 x 300 DPI)